Contributions to the Modeling and Design of Reconfigurable Reflecting Cells Embedding Discrete Control Elements

Julien Perruisseau-Carrier, *Member, IEEE*, Frédéric Bongard, *Member, IEEE*, Ruzica Golubovic-Niciforovic, Roberto Torres-Sánchez, and Juan R. Mosig, *Fellow, IEEE*

***Abstract*—This paper presents new contributions to the modeling and design of reflecting cells embedding discrete control elements such as microelectromechanical system (MEMS) or diodes. First, a rigorous assessment of the different possibilities to simulate and measure the reconfigurable cell in a periodic environment is proposed. Strategies to efficiently model a cell comprising discrete control elements are then presented and discussed in terms of versatility, required assumptions, and computational effort. The most efficient method allows computing all reconfigurable states cell parameters, including information such as the total and dissipated power in each MEMS or diode, in a few minutes using a commercial full-wave solver and adequate post-processing. Finally, the benefit of such an efficient modeling is illustrated by the optimization of an element phase states distribution using a particle swarm optimizer. The concepts presented are also directly applicable to reconfigurable transmitting cells.**

***Index Terms*—Diodes, microelectromechanical system (MEMS), particle swarm optimization (PSO), periodic, reconfigurable, reflectarray, reflecting cell, tunability.**

I. Introduction

REFLECTING cells are key components to various microwave devices such as reflectarrays [1], spatial power combiners [2], or other types of microwave devices requiring the local control of the reflection phase on a reflecting surface [3]. Recently, an effort has been specifically directed toward the implementation of *dynamically reconfigurable* reflecting cells, mainly in the context of reflectarray applications. Indeed, in addition to the known advantages of reflectarrays over parabolic reflectors [1], dynamically controllable reflecting cells would allow electronic reconfigurability. In this context, controllable reflecting cells employing different technologies for microwave reconfigurability have recently been investigated, using ferroelectric thin films [4], liquid crystals [5], photonically controlled semiconductors [6], or varactor diodes [7]–[9]. In addition, there is a particular interest in developing cells based on microelectromechanical system (MEMS) technology [10]–[15], which allows a significant reduction of the losses, intermodulation effects, and dc power consumption, while extending the high-frequency limit of operation for such devices.

Encouraging results on MEMS-based cells have been demonstrated in recent years, e.g., in [10]–[15]. However, much work remains to be done toward the implementation of a viable MEMS-reconfigurable reflective system with overall satisfactory performances. First, works on MEMS reflective cells generally lack a rigorous or comprehensive assessment of their performances, namely, the characterization of all fundamental parameters (e.g., bandwidth, dependence of the phase to the incidence angle, robustness to MEMS fabrication tolerances, cross-polarization, etc.) in realistic simulation or measurement setups. Second, the fact that reconfigurable reflective cells must simultaneously meet numerous requirements implies that good overall performances can only be achieved by efficient design strategies, which have scarcely been discussed thus far.

In this context, this study presents new contributions to the modeling and design of reflective cells, in a general way applicable to most implementations based on discrete control elements such as MEMS or diodes. We first review the different possibilities to account for the periodic environment of the cell in simulation and measurements. The conditions for a rigorous correspondence between the different setups are evaluated, thereby highlighting common misconceptions in reconfigurable reflecting cell characterization. Different strategies to model the MEMS variable elements in a commercial general full-wave simulator are then proposed and compared in terms of versatility and efficiency. In particular, it is shown that modeling the discrete control elements by internal ports and adequate post-processing allows drastic computation time reduction, as well as accessing particular relevant cell parameters such as, e.g., the dissipated power in each MEMS. The reduced simulation time enables cell optimization based on iterative methods requiring the full-wave simulation of the cell at each iteration. As an illustration, we present the optimization of the distribution of the different cell phase states using a particle swarm optimization (PSO) algorithm.

Manuscript received November 18, 2009; accepted December 15, 2009. Date of publication May 18, 2010; date of current version June 11, 2010. This work was supported by the European Union (EU) COST Actions IC0603 and IC0803, and by the Spanish Government Torres Quevedo under Grant PTQ-08-01-06434 and Grant TEC2008-02685/TEC.

J. Perruisseau-Carrier is with the Centre Tecnològic de Telecomunicacions de Catalunya (CTTC), 08860 Castelldefels, Barcelona, Spain (e-mail: julien.perruisseau@cttc.es).

F. Bongard is with JAST SA, Scientific Park of the Ecole Polytechnique Fédérale de Lausanne (EPFL), CH-1015 Lausanne, Switzerland.

R. M. Golubovic-Niciforovic, R. Torres-Sánchez, and J. R. Mosig are with the Laboratoire d'électromagnétisme et d'acoustique (LEMA), Ecole Polytechnique Fédérale de Lausanne Ecole Polytechnique Fédérale de Lausanne (EPFL), CH-1015 Lausanne, Switzerland.

Color versions of one or more of the figures in this paper are available online at http://ieeexplore.ieee.org.

Digital Object Identifier 10.1109/TMTT.2010.2048249

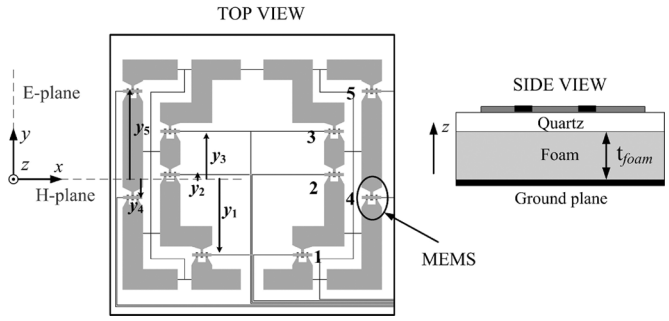

Fig. 1. View of the cell proposed in [16] and used here to illustrate the presented concepts. The element consists of two pseudoring loaded with two-state MEMS variable series capacitors.

II. Description of the Test Cell

This section briefly outlines the reconfigurable reflecting cell used throughout this paper to illustrate the presented concepts. The single-polarized X-band MEMS-reconfigurable cell of [16], shown in Fig. 1, was chosen. This cell was selected as a test case due to its high performance, but principally because a close agreement between simulations and measurement was demonstrated in [16]; since the simulation method used in [16] is one of the methods compared here (more precisely, it is the *detail geometry* simulation of Section IV-C), no further experimental validation is needed in this work. The cell is monolithic and consists of two pseudoring elements loaded with two-state series MEMS capacitors, which allows a dynamic reconfiguration of the reflection phase at a given frequency by affecting the resonance frequency of the pseudorings. The rings are loaded by $N = 5$ pairs of MEMS operated in a binary manner; hence, providing $2^N = 32$ discrete phase states. This digital approach was employed in [16] to allow good MEMS stability, and thus, large phase ranges while guaranteeing good robustness to inherent MEMS fabrication tolerances, temperature drift, and control voltage imprecision.

III. Characterization of Reconfigurable Reflective Cells

This section reviews the different possibilities to rigorously characterize the plane wave reflection coefficient ρ of a cell by simulation or measurement. The required assumptions for each method are clearly exposed to lift common misconceptions in the characterization of such cells.

The reflection coefficient of a reflective element is computed in an infinite periodic environment. This constitutes an approximation whose significance depends on the application, but is the only solution at the cell design stage since the actual cell environment is not known until the design of the whole reflecting surface is completed (see, e.g., [1] for reflectarrays). The infinite array environment is emulated by loading a waveguide (WG) with one or several unit cells, as illustrated in Fig. 2. There are different types of WGs possible for such a characterization, which differ by the boundary conditions imposed on their lateral walls. In order to assess and compare these different characterization methods, we focus on the case of interest here, which is: 1) a cell operating in linear polarization with incident E-field along y and repeated by translation in a rectangular lattice (see Fig. 2) and 2) an incident wave vector $\mathbf{k}$ in the xz-plane.

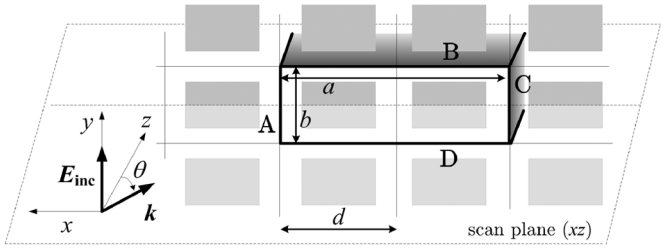

Fig. 2. Characterization of a cell in a WG emulating an infinite periodic environment (the WG considered here is a virtual WG with any boundary conditions on its sidewalls). In the sketch, two cells are embedded in the WG, and the incident field and rectangular lattice depicted are those considered in this study.

A compact overview of the different WG that can be used to model the cell in such a setup is provided in Table I. In each case, the boundary conditions on the sidewalls of each WG are described, along with the required assumptions on the incidence angle and on the element itself, deduced from our analysis.

For the most general and comprehensive characterization of the cell, it must be simulated using periodic boundary conditions (PBCs), as known from Floquet's theorem. The corresponding virtual WG is referred to here as the PBC-WG, in which the incident and reflected fields are expanded into so-called Floquet harmonics [17]. By placing only one cell in the PBC-WG, and assuming that the array lattice simulated corresponds to a reflectarray free of grating lobes for any scan angle above the ground plane ($d < \lambda_0/2$), the PBC-WG supports two orthogonal nonevanescent Floquet harmonics, which provides information on the co- and cross-polarization of the element. In summary, the PBC-WG: 1) allows the characterization of the reflection on the cell for any incidence angle and polarization of the incident field; 2) provides information to deduce the cross-polarization in the specular reflection angle; and 3) does not require assumptions regarding the symmetry of the element.

Table I also describes alternative ways for the characterization of a linearly polarized element, using perfect electric conductor (PEC) and perfect magnetic conductor (PMC) boundaries, or only PECs (referred to as PECPMC and rectangular waveguide (RWG) in this table, respectively). As shown in Table I, the possibility to use a particular characterization setup depends on the incidence angle, on whether the element is symmetrical or not, and on the solver capabilities (e.g., availability of PBCs). Note that the case where all WG walls are PECs (RWG) is the only solution for experimental characterization of the cell in its periodic environment. This well-known concept [18], yet sometimes not rigorously employed, is discussed in some more detail in the Appendix.

IV. Efficient Cell Full-Wave Simulations

A. Introduction

The modeling and optimization of a reconfigurable cell requires a very large number of simulations. For example, in the case of the element introduced in Section II, there are $2^N = 32$ different states to be simulated for several frequency points and incidence angles. Moreover, each of these simulations requires an intensive computational effort since each cell comprises $2N = 10$ MEMS structures. In a process of test and optimization, these simulations must be repeated for each variation

TABLE I
SUMMARY OF CELL SIMULATION/MEASUREMENT POSSIBILITIES IN THE SETUP OF FIG. 2. ACRONYMS: (RECTANGULAR) WAVEGUIDE: (R)WG, PERIODIC BOUNDARY CONDITIONS: PBC, PERFECT ELECTRIC CONDUCTOR: PEC, PERFECT MAGNETIC CONDUCTOR: PMC, TRANSVERSE ELECTROMAGNETIC: TEM

	Type of WG (Boundary conditions)	WG mode	Condition on element	Availability
$\theta = 0$	PBC with $\theta = 0$	Floquet modes (TEM)	-	Simul. only (requires PBC)
	PECPMC (A/C = PMC, B/D = PEC)	TEM	Double symmetry	Simul. only (requires PMC)
$\theta \neq 0$	PBC with $\theta \neq 0$	Floquet modes	-	Simul. only (requires PBC)
	RWG (A/C = PEC, B/D = PEC)	TE_{10}	Double symmetry	Simul. + Measurement

in the design, which is practically prohibitive. In this context, this section first describes the major steps taken to drastically reduce the computation time using Ansoft Corporation's commercial solver High Frequency Structure Simulator (HFSS). The simulation methods are validated using the MEMS element of Fig. 1, which will also serve to illustrate some statements of Section III.

B. PBC-WG and PECPMC-WG Simulations

As explained in Section III, the simulation of an asymmetric reflective cell in a periodic environment requires the use of PBCs, which allow characterization for any incidence angle and frequency. However, an element can, in general, be designed under normal incidence $(\theta = 0°)$ and subsequently characterized under oblique incidence as well. In this case, the computation time in the design stage is reduced by the use of the PECPMC-WG (Table I). The only approximation resulting from this simplification in the case of the element of Fig. 1 is that its small asymmetry around the H-plane is neglected. The impact of this approximation can be assessed by comparing the results obtained with the PBC-WG with $\theta = 0°$ and with the PECPMC-WG, as done in Fig. 3. Both curves are indistinguishable, which confirms that the asymmetry around the H-plane is negligible while validating the proposed equivalence. In terms of computation time, the advantage of replacing the PBC by PEC and PMC boundaries is twofold. First, PEC and PMC boundaries are treated much more efficiently than PBCs by Ansoft HFSS. Second, since the cell is symmetrical around its E-plane, the structure simulated in the PECPMC-WG can be cut in half to further reduce the computational effort.

The designed element can subsequently be characterized under oblique incidence using the PBC-WG, and corresponding results are shown in Fig. 3 for $\theta = 30°$ and $60°$. It reveals that the reflection phase for $\theta = 30°$ already significantly differs from the case of normal incidence since the phase difference reaches $20°$ in some parts of the band. The dependence of the reflection phase to the incidence angle θ significantly increases with θ. This is verified here by observing the large phase discrepancy—from $30°$ to $50°$ for most frequencies—of the case $\theta = 60°$ with regard to normal incidence. These observations, in conjunction with the discussion provided in the Appendix, demonstrate that the RWG method [18] cannot, in general, be used to characterize the reflection phase under normal incidence [e.g., a standard X-band RWG at 8 GHz provides the reflection phase for $\theta = 55.1°$, see (9)].

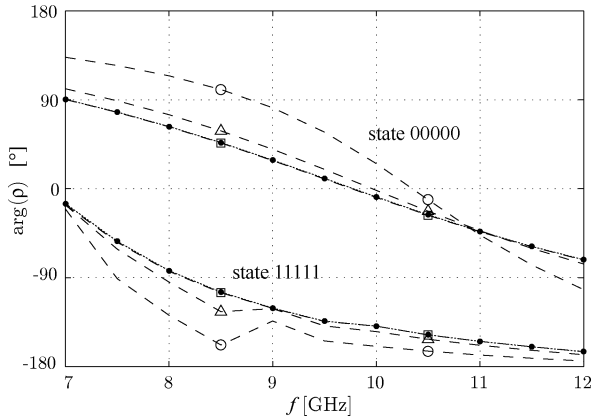

Fig. 3. Comparison of the computed reflection phase of the PECPMC-WG ($\cdots\bullet\cdots$) with that of the PBC-WG for angles of incidence $\theta = 0°$ ($\square$), $\theta = 30°$ ($\triangle$), and $\theta = 60°$ ($\circ$). For clarity, the data are plotted only for the two extreme states and for $t_{\mathrm{foam}} = 3$ mm.

C. MEMS Modeling in Full-Wave Simulation

Including the actual MEMS structures in the full-wave cell model leads to very intensive simulations, since there are $2N = 10$ ($N = 5$, respectively) detailed MEMS geometries to include in the simulated cell with PBCs (PECPMC, respectively). This is not acceptable for an efficient design procedure. However, the small electrical size of the MEMS allows their modeling by lumped-element circuits [19]. In order to deduce these models, simulations of isolated MEMS structures are carried out together with proper parasitics treatment, and are followed by circuit extractions. These two-port simulations are defined to correspond to the actual MEMS environment within the cell, i.e., with the MEMS loading a microstrip of the width of the rings elements and on the same substrate. For the test element of Fig. 1, it was found that the MEMS series capacitor can be accurately modeled in the whole band of interest by, in the up state, a series RC network with $R = 0.3\,\Omega$ and $C = 38$ fF, and, in the down state, by a series RLC network with $R = 0.3\,\Omega$, $L = 150$ pH, and $C = 1500$ fF.

The circuit model of the MEMS can be introduced in the finite-elements' full-wave simulation in two different ways. In the first one, the lumped elements are represented by surface impedance boundaries (*impedance boundaries* method), which already allows a drastic computation time saving with regard to the detailed MEMS geometry. However, it is still necessary to solve for each state of the reconfigurable device, as well as for each variation of the loading element.

In this context, a more powerful approach, referred to here as the *internal ports* method, can be employed. It consists in replacing the surface impedance sheets by internal ports in the

simulation. In this case, the full-wave simulation is run only once and the ports representing the MEMS are loaded by given circuit models in post-processing of the obtained multiport S-matrix. As a result, a single and low-complexity simulation can be carried out for all states and all design variations of the loading MEMS elements, opening the path to an efficient optimization of the structure.

Here, we provide the formulas to perform such a port loading in the general case of a simulation using PBCs (PBC-WG of Section III). In this case, the simulation of a unit cell comprises $M = N + 1$ ports if N MEMS are present in the simulated structure (the remaining port accounting for the incoming/reflected wave on the cell). However, the dimension of the corresponding S-matrix is $M = N + 2$ since the PBC-WG guiding the incoming/reflected wave actually supports two orthogonal Floquet harmonics.

First, we define the general M-port S-matrix $\mathbf{S}$ with ports #1 and #2 corresponding to the Floquet harmonics and ports #3 to #M to the variable loading elements. We can write the scattering system $\mathbf{b} = \mathbf{Sa}$ according to subvectors (and submatrices) corresponding to the unloaded and loaded ports as follows:

$$\begin{bmatrix} \mathbf{b}_{12} \\ \mathbf{b}_{3M} \end{bmatrix} = \begin{bmatrix} \mathbf{S}_A & \mathbf{S}_B \\ \mathbf{S}_C & \mathbf{S}_D \end{bmatrix} \begin{bmatrix} \mathbf{a}_{12} \\ \mathbf{a}_{3M} \end{bmatrix} \tag{1}$$

where $\mathbf{a}_{12}$ and $\mathbf{b}_{12}$ ($\mathbf{a}_{3M}$ and $\mathbf{b}_{3M}$, respectively) are vectors of dimension 2×1 ($(M-2) \times 1$, respectively) and the matrices $\mathbf{S}_A, \mathbf{S}_B, \mathbf{S}_C$ and $\mathbf{S}_D$ of dimensions $2 \times 2, 2 \times (M-2)$, $(M-2) \times 2$ and $(M-2) \times (M-2)$, respectively.

Second, we define the diagonal matrix $\mathbf{\Gamma} = \mathrm{diag}(\rho_3, \rho_4, \ldots, \rho_M)$ comprising the reflection coefficients ρ_m at port m. These reflection coefficients are defined "towards the loads" and are given by $\rho_m = (Z_{L,m} - Z_{\mathrm{ref},m})/(Z_{L,m} + Z_{\mathrm{ref},m})$, where $Z_{L,m}$ and $Z_{\mathrm{ref},m}$ are the loading and reference impedances at port m, respectively. Thus, we have

$$\mathbf{a}_{3M} = \mathbf{\Gamma} \mathbf{b}_{3M}. \tag{2}$$

Now, introducing (2) in (1), after some calculations we obtain

$$\mathbf{b}_{12} = \underbrace{[\mathbf{S}_A + \mathbf{S}_B \mathbf{\Gamma} (\mathbf{I} - \mathbf{S_D} \mathbf{\Gamma})^{-1} \mathbf{S_C}]}_{\mathbf{S}_L} \mathbf{a}_{12} \tag{3}$$

where $\mathbf{I}$ is the identity matrix of dimension M-2. The matrix defined as $\mathbf{S}_L$ in (3) is thus the desired two-port S-matrix linking incident and reflected Floquet harmonics, from which the phase and amplitude of the co- and cross-polarized reflected fields can be deduced. Finally, for the sake of completeness and with regard to the developments leading to (3), interested readers are encouraged to consult [20], which presents a simple and efficient algorithm for the calculation of the S-matrix of arbitrary interconnected multiports.

V. Methods Comparison

This section compares the three modeling approaches described in Section IV-C in terms of precision and computation time. The computed reflection phases for the three options are shown in Fig. 4. For clarity, only four representative states are shown, but similar results are obtained for all states. A very good agreement is observed between all three methods, which simultaneously validates the inclusion of the MEMS loadings in the cell simulation, the "isolated" MEMS lumped model extraction, and the loading of the ports in post-processing. Moreover, it is noticeable that these simulation results are experimentally validated since good agreement between measured results and simulation using the *detailed geometry* approach was demonstrated in [16].

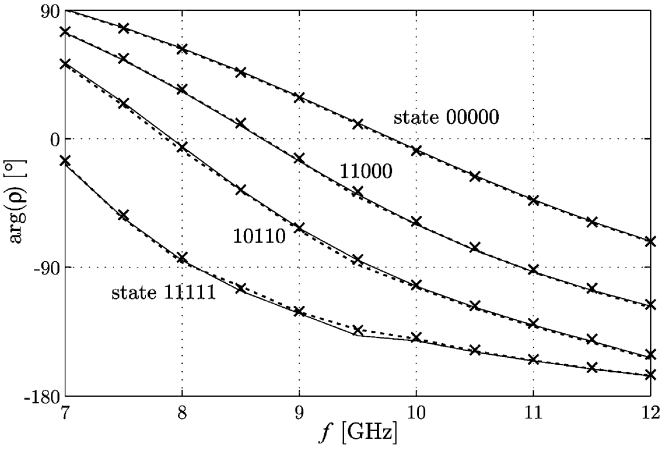

Fig. 4. Comparison of the computed reflection phase with MEMS elements modeled by: (—) their detailed geometry, $(\cdots)$ surface impedance boundaries, $(\times)$ internal ports. For clarity, the data are plotted only for four representative states and correspond to $t_{\mathrm{foam}} = 3$ mm and $\theta = 0°$.

We also compare the three methods in terms of computation time. For fair comparison, first a common precision criterium is defined. As the computation time for each method depends on the number of refinement iterations in the finite-element method, the number of iterations selected for the comparison is determined according to this common convergence criterium. Here, the criterium selected is that the average phase difference of the selected iteration with regard to any subsequent one is below 1°.

All simulations were run for normal incidence using the PECPMC-WG, which is the fastest way to simulate the structure (see Section IV-B). A quad-core 2.86-GHz PC with 8 GB of memory is used. In the case of the *detailed geometry* approach, the simulation of a single state requires about 50 min; hence, 27 h to compute all 32 states. Note that this simulation time is already minimized by the use of the PECPMC-WG and the definition of all conductors as 2-D patterns. Moreover, the high-resistivity dc-biasing lines and the etch holes in the MEMS bridges were removed from the simulations after verification of their negligible effect.

Replacing the detailed MEMS geometry by *impedance boundaries* reduces the simulation time to about 2.5 h for all states; hence, a time saving of a factor 11. A more drastic time reduction is obtained using the *internal ports* method since this one only requires a single simulation of about 6 min, sufficient to compute all 32 states. Thus, this method allows the reduction of the computation time by a factor of about 300 compared to the detailed MEMS geometry description. The only parameter that will significantly impact on the aforementioned *ratios* of simulation times is the number of bits considered. Indeed, both *detailed geometry* and *impedance boundaries* methods

computation times are proportional to the number of states, while the *internal ports* method is almost independent of the number of internal ports. Finally, another advantage of the *internal ports* method is the possibility to model the lumped elements by general impedances rather than equivalent circuits.

As mentioned previously, the general topic of MEMS modeling in full-wave simulation was addressed in [21]. A significant difference between the approach proposed here and [21] is that we model a whole MEMS by a single lumped model in the simulation, whereas [21] proposes to model different parts of the MEMS structures by different networks. Therefore, the proposed approach is much less complex to set up (a simple extraction on the isolated MEMS simulation/measurement is sufficient), and less computational intensive since less ports have to be included in the full-wave simulation. Finally, the precision of our method demonstrates that modeling the whole MEMS by a single lumped model is also valid when the MEMS are inserted within a radiating element, in contrast to the statement of [21]. Compared now to [11], this work is based on commercial software (Ansoft HFSS), whereas [11] implemented a homemade tool for reflecting cells. In addition to demonstrating that such an approach can also be applied to a tool available to the scientific community, the advantage of the use of HFSS is that some strongly limiting assumptions of the simulator of [11] are not required, thanks to the availability of PBCs and the definition of arbitrary geometries and materials. Finally, the possibility of also simulating the detailed MEMS geometry with HFSS allowed the demonstration of the validity and precision of the method.

VI. Additional Cell Parameters Calculation

In Section IV-C, ports #3 to #M were loaded to deduce the 2×2 scattering matrix $\mathbf{S_L}$ linking incident and reflected fundamental Floquet's harmonics on the cell, which provides information for the computation of co- and cross-polarization phases and amplitudes. In practice, it is useful to also compute additional parameters such as, e.g., the dissipation or power to be withstood by the MEMS or diodes for a given plane wave excitation. For instance, let us consider a single-polarized reflectarray cell under normal incidence. In this case, power is fed to port #1 of the overall multiport scattering matrix S (corresponding here to the co-polarized field orientation). Assuming that the reflected cross-polarized field is radiated in free space, we can simply set that the reflection coefficient is zero at this port; hence, $\rho_2 = a_2/b_2 = 0$.

Concerning the remaining ports, corresponding to the MEMS, they are again characterized by (2). Thus, we can calculate the input and output wave vectors $\mathbf{a}$ and $\mathbf{b}$ as a function of the incident amplitude a_1 at the co-polarized port, to compute the power at each MEMS (see below). The procedure is similar to the one of Section IV-C, but we partition the general scattering matrix $\mathbf{S}$ according to the first port only

$$\begin{bmatrix} b_1 \\ \mathbf{b}_{2M} \end{bmatrix} = \begin{bmatrix} S_{A\alpha} & \mathbf{S}_{B\alpha} \\ \mathbf{S}_{C\alpha} & \mathbf{S}_{D\alpha} \end{bmatrix} \begin{bmatrix} a_1 \\ \mathbf{a}_{2M} \end{bmatrix} \tag{4}$$

where a_1 and b_1 ($\mathbf{a}_{2M}$ and $\mathbf{b}_{2M}$, respectively) are of dimension 1×1 ($(M-1)\times 1$, respectively) and $S_{A\alpha}$, $\mathbf{S}_{B\alpha}$, $\mathbf{S}_{C\alpha}$ and $\mathbf{S}_{D\alpha}$ of dimensions 1×1, $1 \times (M-1)$, $(M-1)\times 1$, and $(M-1)\times(M-1)$, respectively. The loading of the #2 to #M ports is

$$\mathbf{a}_{2M} = \mathbf{\Gamma}_\alpha \mathbf{b}_{2M} = \mathrm{diag}(0, \rho_3, \rho_4, \ldots, \rho_M)\mathbf{b}_{2M} \tag{5}$$

with ρ_m, as defined in Section IV-C. Using (4) and (5), we find all loaded ports incident waves as a function of the cell excitation a_1

$$\mathbf{a}_{2M} = \mathbf{\Gamma}_\alpha(\mathbf{I} - \mathbf{S}_{D\alpha}\mathbf{\Gamma}_\alpha)^{-1}\mathbf{S}_{C\alpha}\mathbf{a}_1 \tag{6}$$

as well as reflected ones

$$\mathbf{b}_{2M} = \mathbf{S}_{C\alpha} a_1 + \mathbf{S}_{D\alpha}\mathbf{a}_{2M}. \tag{7}$$

Therefore, all incident and reflected waves are known at each port, and it is possible to identify the power in any of the structure components using well-known scattering expressions. For instance, the power dissipated in each individual MEMS is $L_m = |b_m|^2 - |a_m|^2$, for ports #3 to #M. The loss in the cross-polarized reflected field or by dissipation in the cell materials is calculated in the same manner. Note that the method has been successfully applied to the analysis of the loss in a cell comprising a multitude of MEMS elements in [22], which did not provide the mathematical framework detailed in this section. Finally, the method similarly allows the computation of the RF voltage to be withstood by each MEMS, which is fundamental to assess potential MEMS breakdown or self-actuation [19].

VII. PSO Phase Distribution Optimization

This section further illustrates the benefit of the very fast, but accurate computation of the cell parameters. We present the optimization of a cell *phase distribution*, which represents the repartition of the different reconfigurable reflection phase states at a given frequency. In practice, a linear phase distribution is desired to minimize phase quantization errors.

Some relevant information about this issue can be found in [23] and [24], the latter reference implementing a simple, but limited method for the optimization of the cell phase distribution. Here, we present the application of a global algorithm for such optimization, which does not suffer from the strongly limiting assumptions of [24]. However, such a global optimization requires the computation of the cell parameters in all states at each iteration, and could only be envisioned thanks to the very fast computation of the cell parameters discussed earlier.

Here a PSO algorithm, which has been successfully applied to electromagnetic (EM) problems in the past [25]–[27], is used. Fig. 5 shows the complete optimizer structure: the optimization loop is driven by the PSO algorithm, while the EM analysis of the reflective cell is done using HFSS. The interface between the PSO algorithm and HFSS is provided by MATLAB, which allows for a proper automation of the exchange and post processing tasks required, as detailed in [28]. More specifically, the post-processing of the full-wave multiport scattering matrix of the cell to obtain the relevant cell parameters, as described in Section IV-C, is also easily implemented in MATLAB and included in the loop prior to the cost function evaluation. The input

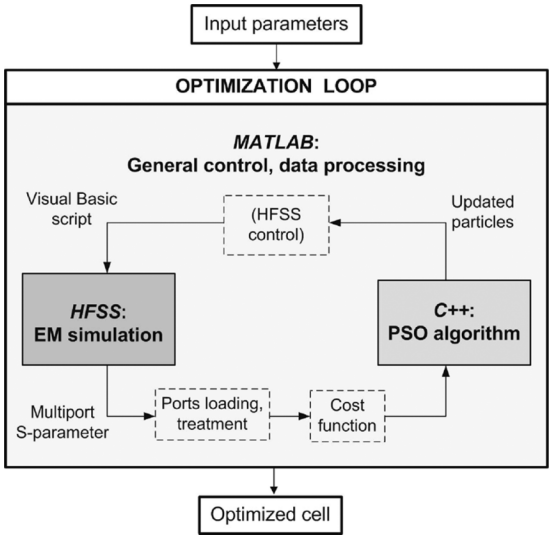

Fig. 5. Flowchart describing the optimization procedure of the digitally reconfigurable reflective cell.

parameters of the procedure are the geometry of the resonant element, the desired overall phase range needed for the concerned application, the operating frequency, as well as the internal settings of the PSO algorithm (variables to be optimized, their respective ranges and the setup of the PSO parameters). The stopping criteria is either a cost-function threshold or a maximum number of optimization iterations.

The cost-function C associated with the optimization problem is defined by (8) as the mean square discrepancy between the current phase distribution and the ideal one. The ideal function is linear $f_{\text{ideal}}(s) = A(s-1) + B$, which minimizes phase quantization errors, where s is the index of a given state after sorting all states for a progressive phase distribution of $f_{\text{current}}(s)$, and N is the number of independent digital MEMS in the cell (here $N = 5$). The slope A of f_{ideal} is determined by the target phase range R for the desired application—passed as an input goal to the optimizer—according to $A = R/(2^N - 1)$. Concerning B, it is important to note that, in most applications, only the phase *difference* between the cells of a reflector is relevant. As a result, the offset B of the phase distribution has no impact on the device performance and is, thus, a free parameter. This is fundamental for the cell optimization, so here the cost function is calculated at each iteration for the value of B giving the lowest cost C

$$C = \sum_{s=1}^{2^N} |f_{\text{current}}(s) - f_{\text{ideal}}(s)|^2. \tag{8}$$

The optimization procedure was applied to the test cell used previously in this paper and depicted in Fig. 1. The phase distribution was optimized at 10 GHz for a target phase range of 180°. The PSO setup shown in [25] to lead to the best convergence is used: c_1 and c_2 are equal to 1.5, time-varying c_0 is decreasing from 0.9 to 0.4 over the course of the run, and the maximal velocity $V_{\max}$ is equal to the dynamic range for each dimension of the optimization space. The so-called invisible wall boundary condition is applied to the particles that go outside the optimization space.

TABLE II
OPTIMIZED PARAMETERS OF THE CELL OF FIG. 1 WITH THEIR BOUNDARIES AND OPTIMIZED VALUES AFTER OPTIMIZATION (IN MILLIMETERS)

Optimization param.	name and boundaries	optimized value
Pos. of MEMS 2	$-1.475 \leq y_2 \leq 1.475$	-0.821
Pos. of MEMS 3	$-1.475 \leq y_3 \leq 1.475$	1.176
Pos. of MEMS 4	$-2.975 \leq y_4 \leq 2.975$	2.521
Pos. of MEMS 5	$-2.975 \leq y_5 \leq 2.975$	0.151
Foam subs. thick.	$0.8 \leq t_{foam} \leq 3$	2.562

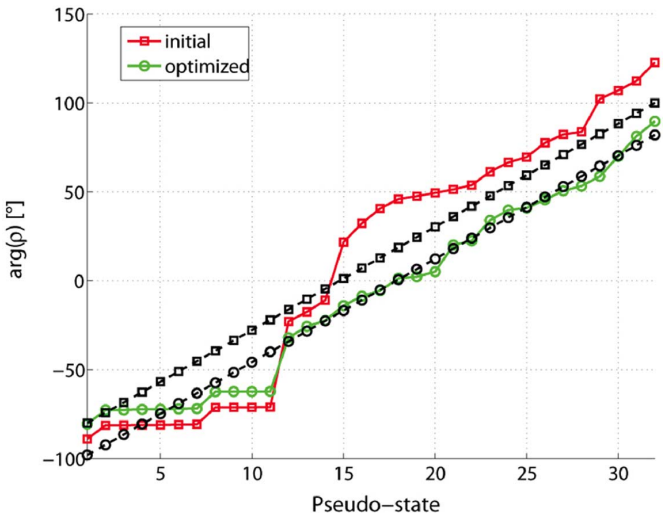

Fig. 6. Initial and optimized phase diagram (—): simulated, (- -): ideal distribution (see text).

The input and optimized parameters of the geometry are summarized in Table II. The positions of MEMS #2 to #5 can be varied along the y dimension, within boundaries set by the metallization geometry, which was let fixed here. The position of MEMS #1 is not optimized since this would imply much complication in the procedure (see the cell geometry in Fig. 1). The thickness of the foam substrate is also optimized since this parameter can easily be chosen in practice and has a direct impact on the phase range of such a resonant cell.

The improvement achieved after 300 evaluations of the cost function is illustrated in Fig. 6, where the initial and the optimized phase distributions are compared to their respective "best offset B" linear goals. The initial phase distribution has been significantly improved and is almost perfect between pseudostates 12 and 32, leading to an average root mean square error of less than 3° for the whole pseudostates range. Although a detailed interpretation and discussion of the optimization based on physical considerations is beyond the scope of this study, we observe here that the remaining part of the phase distribution plot cannot be improved, which is due to a fundamental physical limitation of the device rather than to the optimizer performance.

VIII. CONCLUSION

A strategy to drastically reduce the full-wave computation time of reconfigurable cell embedding discrete elements such as

MEMS or diodes was presented and validated. The method enables full-wave based optimizations for such cells, as exemplified here using a PSO algorithm to linearize the cell phase states distribution. The method was also extended to provide information such as the total and dissipated power in each discrete control element. Although the proposed concepts were discussed here in the context of reflecting cells, they are directly applicable to transmitting cells as well.

APPENDIX A
RWG-BASED CHARACTERIZATION

For the reasons explained at the conclusion of Section III, we provide here some further comments on the characterization of a cell in a RWG. We consider a usual RWG with $a > 2b$ (see Fig. 2) operated in its fundamental TE_{10} mode only. This RWG can be used to characterize the reflection phase of a cell symmetrical around both its x- and y-axes, in the periodic environment of Fig. 2 and for an incidence θ, according to (9) [18] as follows:

$$|\sin\theta| = \frac{\lambda_0}{2a}. \tag{9}$$

This formula is obtained by expressing the TE_{10} mode field distribution as a superposition of two plane waves of same amplitude, same phase along the axis of the RWG, and of opposite incidence angles $+\theta$ and $-\theta$. The number of elements placed in the RWG cross section is not necessarily 1. According to image theory, there can be any number m of half-elements placed in the RWG, so for an array of lattice spacing d

$$a = \left(\frac{m}{2}\right) d, \qquad \text{with } m \in \mathbb{N}^*. \tag{10}$$

Observation of (9) shows that the RWG characterization of a cell is only possible for a given incidence angle at each frequency, which is determined by the choice of m.

In addition, further developments demonstrate additional restrictions to the use of this method. For clarity, let us consider here the reflectarray application, although similar restrictions will apply to other applications of reconfigurable reflective cells. To that aim, we first write the cutoff frequencies of the two first modes of the RWG with $a > 2b$ as

$$f_{10} = 0.5 f_{20} = \frac{c_0}{2a} \tag{11}$$

and note that the condition for excluding grating lobes in a reconfigurable array scanning any angle $[-90°; +90°]$ above the reflector plane is $d < \lambda_0/2$, independently of the incidence angle. Now, using (10), (11), and the condition $d < \lambda_0/2$, we obtain the condition $m \geq 3$ on the number m of half-elements in the RWG. Thus, there must be at least $m/2 = 1.5$ elements in the RWG so that the element and lattice characterized with the fundamental TE_{10} mode correspond to a reflectarray able to scan the desired scan range without grating lobes. Here, we have neglected the possible relaxation of the grating lobes condition due to the element radiation pattern or a limited scan range. However, since $m \in \mathbb{N}^*$, such a relaxation would not impact on the result $m \geq 3$ in most cases. Finally, it is observed that the maximum and minimum incidence angles θ that can be simulated with the monomodal RWG are $\theta_{\max} = \theta(f_{10}) = 90°$ and $\theta_{\min} = \theta(f_{20}) = 30°$.

These considerations lead to the following three main conclusions: First, the characterization of a *single* reconfigurable cell placed in a conventional RWG is not sufficient to assess the performance of the cell because the array lattice thereby characterized does not, in general, correspond to a reflectarray free of grating lobes. Second, since the RWG only allows the characterization of incidence angles $\theta > 30°$, it cannot be considered, in contrast with the statements of [29] and [30], as a fairly good approximation of the reflection phase for other pairs of frequency and angle, and especially for normal incidence $\theta = 0°$. This remark holds for all planar elements, but was illustrated here in Fig. 3 in the case of our test MEMS cell. Third, the RWG-based characterization does not allow a rigorous assessment of the bandwidth of the element since it is not possible to characterize the variation of the reflection phase with frequency for a fixed incidence angle. As a conclusion, rigorous cell characterization requires its simulation in a PBC-WG, while RWG-based measurement represents an efficient way to validate simulations provided comparison with a strict correspondence of lattice, frequency, and incidence angle.

REFERENCES

[1] D. Pozar, S. Targonski, and H. Syrigos, "Design of millimeter wave microstrip reflectarrays," *IEEE Trans. Antennas Propag.*, vol. 45, no. 2, pp. 287–296, Feb. 1997.

[2] R. A. York and Z. B. Popovic, *Active and Quasi-Optical Arrays for Solid-State Power Combining*. New York: Wiley, 1997.

[3] A. R. Weily, T. S. Bird, and Y. J. Guo, "A reconfigurable high-gain partially reflecting surface antenna," *IEEE Trans. Antennas Propag.*, vol. 56, no. 11, pp. 3382–3390, Nov. 2008.

[4] R. Romanofsky, "Advances in scanning reflectarray antennas based on ferroelectric thin-film phase shifters for deep-space communications," *Proc. IEEE*, vol. 95, no. 10, pp. 1968–1975, Oct. 2007.

[5] H. Wenfei, R. Cahill, J. A. Encinar, R. Dickie, H. Gamble, V. Fusco, and N. Grant, "Design and measurement of reconfigurable millimeter wave reflectarray cells with nematic liquid crystal," *IEEE Trans. Antennas Propag.*, vol. 56, no. 10, pp. 3112–3117, Oct. 2008.

[6] M. Chaharmir, J. Shaker, M. Cuhaci, and A.-R. Sebak, "Novel photonically controlled reflectarray antenna," *IEEE Trans. Antennas Propag.*, vol. 54, no. 4, pp. 1134–1141, Apr. 2006.

[7] D. Sievenpiper, J. Schaffner, H. Song, R. Loo, and G. Tangonan, "Two-dimensional beam steering using an electrically tunable impedance surface," *IEEE Trans. Antennas Propag.*, vol. 51, no. 10, pp. 2713–2722, Oct. 2003.

[8] M. Riel and J.-J. Laurin, "Design of an electronically beam scanning reflectarray using aperture-coupled elements," *IEEE Trans. Antennas Propag.*, vol. 55, no. 5, pp. 1260–1266, May 2007.

[9] S. V. Hum, M. Okoniewski, and R. J. Davies, "Modeling and design of electronically tunable reflectarrays," *IEEE Trans. Antennas Propag.*, vol. 55, no. 8, pp. 2200–2210, Aug. 2007.

[10] J. Perruisseau-Carrier, H. Legay, J. Lenkkeri, J.-P. Polizzi, E. Jung, and A. Skrivervik, "A dynamically-controlled reflectarray element using embedded packaged MEMS switches," in *IEEE Int. Antennas Propag. Symp.*, San Diego, CA, 2008.

[11] E. Perret, H. Aubert, and H. Legay, "Scale-changing technique for the electromagnetic modeling of MEMS-controlled planar phase shifters," *IEEE Trans. Microw. Theory Tech.*, vol. 54, no. 9, pp. 3594–3601, Sep. 2006.

[12] S. Hum, G. McFeetors, and M. Okoniewski, "Integrated MEMS reflectarray elements," in *1st Eur. Antennas Propag. Conf.*, Nice, France, 2006.

[13] H. Legay, B. Pinte, E. Girard, R. Gillard, M. Charrier, and A. Ziaei, "A low loss and steerable reflectarray antenna in Ka band," in *27th ESA Antenna Technol. Innovative Periodic Antennas Workshop*, Santiago de Compostela, Spain, 2004, pp. 281–288.

[14] B. Mencagli, R. Gatti, L. Marcaccioli, and R. Sorrentino, "Design of large mm-wave beam-scanning reflectarrays," in *Eur. Microw. Conf.*, Paris, France, 2005.
[15] H. Rajagopalan, Y. Rahmat-Samii, and W. A. Imbriale, "Integration of RF MEMS switches with the reconfigurable reflectarray element: A novel patch-slot implementation," in *IEEE AP-S Int. Symp.*, 2008, pp. 1–4.
[16] J. Perruisseau-Carrier and A. Skrivervik, "Monolithic MEMS-based reflectarray cell digitally reconfigurable over a 360° phase range," *IEEE Antennas Wireless Propag. Lett.*, vol. 7, pp. 138–141, 2008.
[17] M. Bozzi, L. Perregrini, J. Weinzierl, and C. Winnewisser, "Efficient analysis of quasi-optical filters by a hybrid MoM/BI-RME method," *IEEE Trans. Antennas Propag.*, vol. 49, no. 7, pp. 1054–1064, Jul. 1999.
[18] P. Hannan and M. Balfour, "Simulation of a phased-array antenna in waveguide," *IEEE Trans. Antennas Propag.*, vol. AP-13, no. 3, pp. 342–353, Mar. 1965.
[19] G. Rebeiz, *RF MEMS, Theory, Design and Technology*. New York: Wiley, 2003.
[20] P. Hallbjörner, "Method for calculating the scattering matrix of arbitrary microwave networks giving both internal and external scattering," *Microw. Opt. Technol. Lett.*, vol. 38, no. 2, pp. 99–102, Jul. 2003.
[21] P. Arcioni, G. Conciauro, and M. Repossi, "Planar models of reconfigurable MEMS circuits," *IEEE Trans. Microw. Theory Tech.*, vol. 55, no. 4, pp. 722–728, Apr. 2007.
[22] J. Perruisseau-Carrier, E. Girard, and H. Legay, "Analysis of a reconfigurable reflectarray cell comprising a multitude of MEMS control elements," in *4th Eur. Antennas Propag. Conf.*, Barcelona, Spain, 2010.
[23] H. Salti, E. Fourn, R. Gillard, and H. Legay, "Robustness optimization of MEMS-based reflectarray phase-shifting cells," in *3rd Eur. Antennas Propag. Conf.*, 2009, pp. 3724–3728.
[24] J. Perruisseau-Carrier and A. Georgiadis, "Efficient optimization of the phase diagram in digitally-controlled reflective cells," in *3rd Eur. Antennas Propag. Conf.*, Berlin, Germany, 2009, pp. 1230–1233.
[25] J. Robinson and Y. Rahmat-Samii, "Particle swarm optimization in electromagnetics," *IEEE Trans. Antennas Propag.*, vol. 52, no. 2, pp. 397–407, Feb. 2004.
[26] N. Jin and Y. Rahmat-Samii, "Advances in particle swarm optimization for antenna design: Real-number, binary, single-objective and multiobjective implementations," *IEEE Trans. Antennas Propag.*, vol. 55, no. 3, pp. 556–567, Mar. 2007.
[27] B. Fuchs, R. Golubovic, A. Skrivervik, and J. Mosig, "Spherical lens antenna designs with particle swarm optimization," *Microw. Opt. Technol. Lett.*, accepted for publication.
[28] S. López-Peña, J. Zürcher, R. Torres-Sánchez, A. G. Polimeridis, and J. R. Mosig, "Modeling and manufacturing of a series of identical antennas for a P-band ice sounder," in *Proc. 4th Eur. Antennas Propag. Conf.*, 2010.
[29] A. Moessinger, R. Marin, J. Freese, S. Mueller, A. Manabe, and R. Jakoby, "Investigations on 77 GHz tunable reflectarray unit cells with liquid crystal," in *1st Eur. Antennas Propag. Conf.*, Nice, France, 2006.
[30] O. G. Vendik and M. Parnes, "A phase shifter with one tunable component for a reflectarray antenna," *IEEE Antennas Propag. Mag.*, vol. 50, no. 4, pp. 53–65, Aug. 2008.

Julien Perruisseau-Carrier (S'07–M'09) was born in Lausanne, Switzerland, in 1979. He received the M.Sc. and Ph.D. degrees from the Ecole Polytechnique Fédérale de Lausanne (EPFL), Lausanne, Switzerland, in 2003 and 2007, respectively.

In 2003, he was a Visiting Researcher with the Communication Group, University of Birmingham, Birmingham, Edgbaston, U.K. From 2004 to 2007, he was with the Laboratory of Electromagnetics and Acoustics (LEMA), Ecole Polytechnique Fédérale de Lausanne (EPFL), where he completed the doctoral degree while working on various European Union (EU) funded projects. Since December 2007, he has been a Research Associate with the Centre Tecnològic de Telecomunicacions de Catalunya (CTTC), Barcelona, Spain. He has authored over 50 journal and international conference papers. He is a Reviewer for various journals on antennas and microwaves. His research interest mainly concerns reconfigurable microwave devices. In particular, he has been involved in the development of dynamically reconfigurable reflectarrays, antennas, and metamaterials.

Dr. Perruisseau-Carrier was the recipient of the Young Scientist Award of the URSI-EMTS 2007 Conference and of the IEEE AP-S Raj Mittra Travel Grant 2010.

Frédéric Bongard (S'08–M'09) was born in Yverdon, Switzerland, in 1978. He received the M.Sc. degree in electrical engineering and Ph.D. degree from the Ecole Polytechnique Fédérale de Lausanne (EPFL), Lausanne, Switzerland, in 2003 and 2009, respectively.

From 2003 to 2004, he was an Assistant with the acoustics portion of the Laboratory of Electromagnetics and Acoustics (LEMA), EPFL. From 2004 to 2009, he was with the electromagnetics portion of LEMA, where he completed the doctoral degree while working as a Research and Teaching Assistant. Since November 2009, he has been a Research and Development Antenna Engineer with JAST SA, Lausanne, Switzerland. He has been involved in projects for the European Space Agency (ESA) and the European Network of Excellence on metamaterials (Metamorphose). His research interests include metamaterials for microwave applications and antenna arrays.

Ružica Golubović-Nićiforović was born in Belgrade, Serbia, in 1983. She received the Dipl.Ing. degree from the School of Electrical Engineering (ETF), University of Belgrade, Belgrade, Serbia, in 2006, and is currently working toward the Ph.D. degree at the Laboratory of Electromagnetics and Acoustics (LEMA), Ecole Polytechnique Fédérale de Lausanne (EPFL), Lausanne, Switzerland.

Her research interests include computational electromagnetics with an emphasis on planar multilayered media and optimization techniques.

Roberto Torres-Sánchez was born in Granada, Spain, in 1979. He received the Ingeniero de Telecomunicación degree from the Universidad de Málaga, Málaga, Spain, in 2006, and is currently working toward the Ph.D. degree at the École Polytechnique Fédérale de Lausanne (EPFL), Lausanne, Switzerland.

His research interests include EM theory, printed microwave circuits, and antennas.

Mr. Torres-Sánchez was the recipient of the 2006 ASTRA Award for the Best Master Thesis Dissertation from the Spanish Colegio Oficial de Ingenieros de Telecomunicación (COIT).

Juan R. Mosig (S'76–M'87–SM'94–F'99) was born in Cádiz, Spain. He received the Electrical Engineer degree from the Universidad Politécnica de Madrid, Madrid, Spain, in 1973, and the Ph.D. degree from the Ecole Polytechnique Fédérale de Lausanne (EPFL), Lausanne, Switzerland, in 1983.

In 1976, he joined the Laboratory of Electromagnetics and Acoustics, EPFL. Since 1991, he has been a Professor with EPFL. Since 2000, he has been the Head of the Laboratory of Electromagnetics and Acoustics (LEMA), EPFL. In 1984, he was a Visiting Research Associate with the Rochester Institute of Technology, Rochester, NY, and Syracuse University, Syracuse, NY. He has also held scientific appointments with the University of Rennes, Rennes, France, the University of Nice, Nice, France, the Technical University of Denmark, Lyngby, Denmark, and the University of Colorado at Boulder. He is currently the Chairman of the EPFL Space Center, where he is responsible for many Swiss research projects for the European Space Agency (ESA). He has authored five book chapters on microstrip antennas and circuits and over 100 reviewed papers. His research interests include EM theory, numerical methods, and planar antennas.

Dr. Mosig is a member of the Swiss Federal Commission for Space Applications. He is currently a member of the Board of the Applied Computational Electromagnetics Society (ACES). He is chairman of the European COST Project on Antennas ASSIST (2007–2011). He is a founding member and acting chair of the European Association and the European Conference on Antennas and Propagation (EurAAP and EuCAP).